Received: 18 November 2016 | Revised: 7 May 2017 | Accepted: 9 May 2017

DOI: 10.1002/eqe.2925

RESEARCH ARTICLE

WILEY

Nonlinear FE model updating and reconstruction of the response of an instrumented seismic isolated bridge to the 2010 Maule Chile earthquake

Yong Li[1] | Rodrigo Astroza[2] | Joel P. Conte[3] | Pedro Soto[4]

[1] Department of Civil and Environmental Engineering, University of Alberta, Edmonton, Canada

[2] Facultad de Ingeniería y Ciencias Aplicadas, Universidad de los Andes, Santiago, Chile

[3] Department of Structural Engineering, University of California, San Diego, La Jolla, CA, USA

[4] Departamento de Ingeniería Civil, Universidad de Chile, Santiago, Chile

Correspondence
Joel P. Conte, Department of Structural Engineering, University of California, San Diego, La Jolla, CA 92093, USA.
Email: jpconte@ucsd.edu

Funding information
Pacific Earthquake Engineering Research Center's Transportation Systems Research Program, Grant/Award Number: 1107-NCTRCJ; UCSD Academic Senate, Grant/Award Number: RN091G-CONTE; Chilean National Commission for Scientific and Technological Research (CONICYT), Grant/Award Number: 11160009

Summary

Nonlinear finite element (FE) modeling has been widely used to investigate the effects of seismic isolation on the response of bridges to earthquakes. However, most FE models of seismic isolated bridges (SIB) have used seismic isolator models calibrated from component test data, while the prediction accuracy of nonlinear FE models of SIB is rarely addressed by using data recorded from instrumented bridges. In this paper, the accuracy of a state-of-the-art FE model is studied through nonlinear FE model updating (FEMU) of an existing instrumented SIB, the Marga-Marga Bridge located in Viña del Mar, Chile. The seismic isolator models are updated in 2 phases: component-wise and system-wise FEMU. The isolator model parameters obtained from 23 isolator component tests show large scatter, and poor goodness of fit of the FE-predicted bridge response to the 2010 Mw 8.8 Maule, Chile Earthquake is obtained when most of those parameter sets are used for the isolator elements of the bridge model. In contrast, good agreement is obtained between the FE-predicted and measured bridge response when the isolator model parameters are calibrated using the bridge response data recorded during the mega-earthquake. Nonlinear FEMU is conducted by solving single- and multiobjective optimization problems using high-throughput cloud computing. The updated FE model is then used to reconstruct response quantities not recorded during the earthquake, gaining more insight into the effects of seismic isolation on the response of the bridge during the strong earthquake.

KEYWORDS

2010 Maule earthquake, bridge, bridge system response prediction accuracy, nonlinear finite element model updating, optimization, seismic isolation

1 | INTRODUCTION

Highway bridges, critical components of transportation networks, have been recognized as among the most vulnerable structures to natural disasters, especially to earthquakes.[1] Recent earthquakes have further shown the vulnerability of bridges and emphasized the importance of ensuring a satisfactory seismic performance of such structures in future earthquakes.[2] Consequently, seismic protection systems, such as low-damage and damage-free resilient design strategies (eg, seismic isolation and self-centering systems), have become attractive and popular technologies to mitigate the damaging effects of earthquakes on bridges and, therefore, enhance their seismic performance.[3,4] In particular, seismic isolation provides a flexible horizontal

interface with high internal damping, typically located between the top of the piers/abutment stem walls and the bridge superstructure. This results in the elongation of the fundamental period of the bridge, moving it away from the range of dominant frequencies of earthquake excitation, and the increase of the energy dissipation capacity of the bridge system. The excellent performance of isolated bridges during recent earthquakes has demonstrated the effectiveness of seismic isolation and especially of rubber bearings.[5,6] However, limited investigation of seismic isolated bridge (SIB) structures has been performed using data recorded in situ during strong earthquakes, mainly because of the scarcity of this type of data. Comprehensive comparative studies using data recorded from laboratory component tests and from instrumented SIB structures during earthquakes are even more limited.

Nonlinear finite element (FE) modeling and response simulation has now become an important tool in seismic design, condition assessment, and performance prediction of large and complex civil structures (eg, buildings and bridges) under various loads. To validate nonlinear FE models of structures subjected to seismic excitation, experimental data recorded under realistic conditions of the structure and dynamic excitation must be used. In this regard, shake table tests of large- or full-scale building specimens have provided unique and important data.[7] However, for bridge structures, it is unfeasible to conduct large- or full-scale experiments under realistic conditions (eg, multiple-support excitation and interaction between bridge deck and abutments). The one-fourth scale 2-span, 3-bent reinforced concrete (RC) bridge tested at the University of Nevada, Reno, using a shake table array is probably the most complex seismic test program conducted on bridges.[8] Although this experimental program represents a significant effort in approaching real-world conditions, experimental tests of bridge components and subassemblies do not allow to fully characterize the behavior of a whole bridge system, which includes the interactions between its different components. Unfortunately, data recorded on bridge structures, including those with seismic isolation, during strong earthquakes are scarce, and very limited research has been performed on comparative or correlation studies between field recorded and FE-predicted seismic responses of bridges (eg, previous studies[9,10]).

Although significant advances have been made in the field of computational structural mechanics (eg, inelastic material constitutive models and nonlinear solution strategies), the accuracy of nonlinear FE models of large and complex real-world civil structures (eg, bridges) subjected to strong earthquake excitation needs to be investigated further and validated. A nonlinear FE model of a structure depends on a set of highly uncertain parameters[11] (eg, material parameters and boundary conditions) and, consequently, needs to be calibrated to minimize the discrepancy between the FE-predicted and measured responses of the structure. This process is known as FE model updating (FEMU). In recent years, several methods for updating nonlinear FE models of civil structures have been developed and mostly applied to highly (overly) simplified nonlinear structural models and numerically simulated data or experimental data from small-scale structural specimens (eg, other studies[12,13]).

The nonlinear FEMU process requires many evaluations of the FE model, and sequential evaluations may therefore be computationally prohibitive for large and complex civil structures. In contrast, an alternative nonlinear FEMU approach is promoted in this paper by virtue of the cloud-based high-throughput distributed computing technologies (eg, previous studies[14,15]), which enable a grid-based correlation study between FE-predicted and measured structural responses. This grid-based correlation approach conducts the updating of state-of-the-art structural FE models of complex civil structural and/or geotechnical systems in a significantly reduced time, especially in the case of low-dimensional modeling parameter space.

In this paper, the acceleration response data recorded on the Marga-Marga Bridge during the 2010 Mw 8.8 Maule, Chile earthquake are used to update a nonlinear FE model of the bridge developed in the FE analysis software framework OpenSees,[16] with a focus on isolator model parameters. This FE model includes multiple-support seismic excitation (ie, inputs at the base of the bridge piers different from those at the bridge ends). First, the experimental data from component tests on prototypes of the high-damping rubber bearings (HDRBs) of the bridge are used to estimate the parameters of the isolator model. Using these parameter estimates for the seismic isolator model and the FE model of the bridge, the FE-predicted response is then compared to the measured response of the bridge to the Maule Earthquake. Next, the data recorded on the bridge are used to update the seismic isolator parameters of the bridge model. Three primary parameters (ie, initial stiffness, yield strength, and postyield to preyield stiffness ratio) describing the nonlinear behavior of the rubber bearings (the main source of nonlinearity in the bridge during the Maule earthquake as verified in this study) are updated, because they are the most influential parameters on the recorded response of the bridge.

2 | DESCRIPTION OF THE BRIDGE AND INSTRUMENTATION

2.1 | Bridge description

The Marga-Marga Bridge (Figure 1), located in the city of Viña del Mar, is the first SIB constructed in Chile. It is a continuous straight highway bridge, consisting of 8 spans for a total length of 383.0 m. The elevation and plan views

FIGURE 1 Photo of the Marga-Marga Bridge in Viña del Mar, Chile [Colour figure can be viewed at wileyonlinelibrary.com]

of the bridge are shown in Figure 2. The bridge superstructure is composed of a RC deck with constant cross section (0.27 m thick by 18.0 m wide) supported by 4 continuous I girders made of ASTM A-242-81 steel.

The bridge superstructure is supported by 7 piers (single-column bents) and 2 abutments. Five intermediate piers, P#2 to P#6, are supported on pile-group foundations, while the other 2 piers, P#1 and P#7, and both abutments are supported on shallow foundations. The pier columns have varying heights, denoted as H, measured from the top of the foundation cap to the bottom of the pier cap beam, ranging from 21.9 m (P#1) to 30.2 m (P#6). The pier columns have a double-cell RC box section with dimensions of 2.0 m wide by 10.0 m deep and are oriented with their weak axis bending perpendicular to the longitudinal direction of the bridge (see Figure 3a). Concrete with a nominal compressive strength of 25.0 MPa and reinforcing steel with a nominal yield strength of 420.0 MPa were used for the pier columns. At the bridge ends, the superstructure is restrained in the transverse direction by stoppers with the contact steel plates greased to allow free movement in the longitudinal direction through finger joints spanning over a gap of 0.3 m. The dimensions of the foundation caps ($B \times H_1$) are shown in Figure 3a. The foundation piles have a circular cross section with a diameter of 1.0 m and their lengths range between 14.02 and 32.40 m (see Figure 2). All the foundation piles are fully embedded in the soil, which consists of layers of silty sand overlaying gravel and spots of clay.

2.2 | Instrumentation setup and monitoring system

A seismic monitoring system consisting of 24 accelerometers was installed in the free field and on the structure (see Figures 2 and 3a) to record the earthquake ground motion and dynamic response of the bridge and to investigate the bridge behavior during earthquakes.[17] The system consists of an 18-channel central recording system Kinemetrics Altus Mt. Whitney equipped

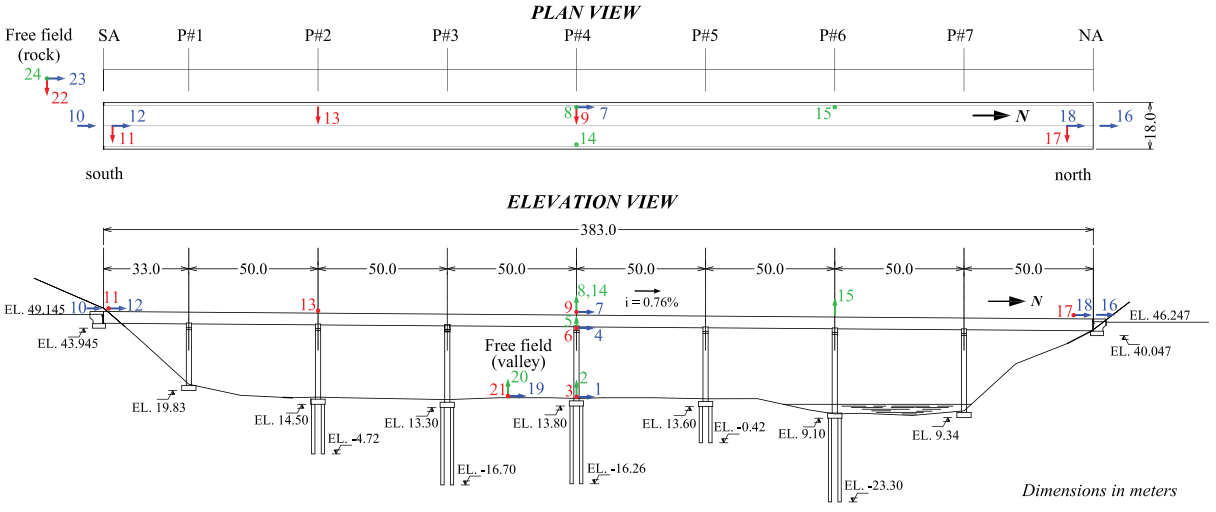

FIGURE 2 Plan and elevation views and instrumentation of the Marga-Marga Bridge. NA, North abutment; SA, South abutment [Colour figure can be viewed at wileyonlinelibrary.com]

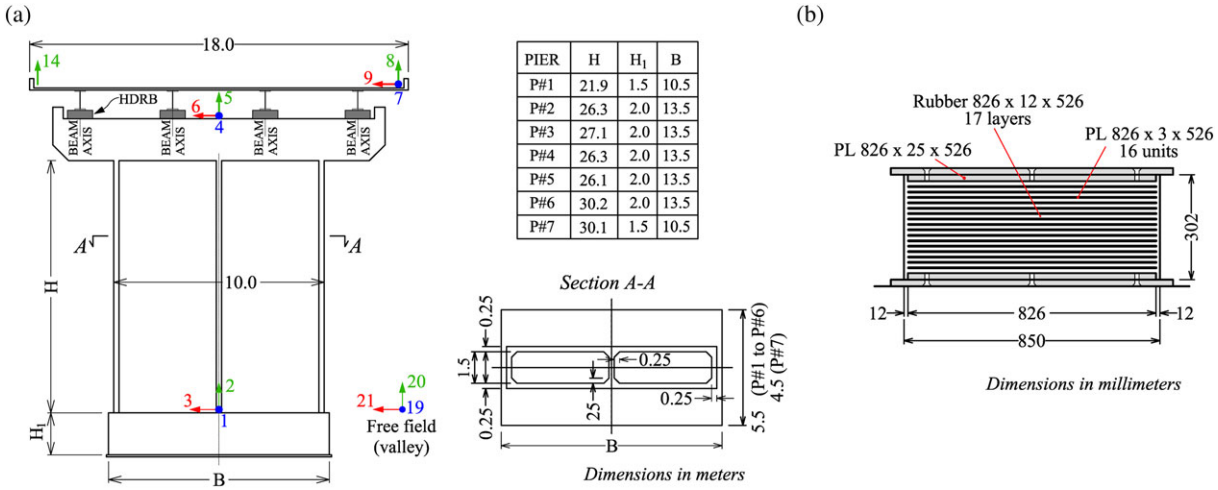

PIER	H	H_1	B
P#1	21.9	1.5	10.5
P#2	26.3	2.0	13.5
P#3	27.1	2.0	13.5
P#4	26.3	2.0	13.5
P#5	26.1	2.0	13.5
P#6	30.2	2.0	13.5
P#7	30.1	1.5	10.5

FIGURE 3 (a) Pier columns and instrumentation, and (b) HDRB (seismic isolator) on bridge piers. HDRB, high-damping rubber bearing [Colour figure can be viewed at wileyonlinelibrary.com]

with a GPS timing system (accuracy of 5 μs). Three triaxial Kinemetrics FBA-23 (channels 1-9 in Figure 2) and 9 uniaxial Kinemetrics FBA-11 accelerometers (channels 10-18 in Figure 2) are connected to this recording system. In addition, a Kinemetrics Altus Etna accelerograph with one triaxial Kinemetrics FBA-23 accelerometer (channels 19-21 in Figure 2) is installed in free-field conditions in the valley and connected by a local network to the central recording system. A Kinemetrics QDR accelerograph is located close to the South abutment (SA) (channels 22-24 in Figure 2) in free-field conditions but is not synchronized with the other sensors. Channels 1 to 18 are installed on the bridge structure, ie, at the bottom and top of bridge pier P#4, on the bridge deck over piers P#2, P#4, and P#6, at both bridge ends, and at both abutments. To summarize, the instrumentation of the bridge structure consists of 7 channels, 5 channels, and 6 channels, in the longitudinal, vertical, and transverse directions of the bridge (see Figures 2 and 3a), respectively. The accelerometers are force balance acceleration sensors with a dynamic range of 135 dB from 0.01 to 50 Hz and 145 dB from 0.01 to 20 Hz and a frequency bandwidth DC—100 Hz. The records were sampled at 100 Hz for the sensors installed in the free field at the SA and at 200 Hz for the others.

Seismic isolation, with a total of 36 rectangular HDRBs (seismic isolators), was incorporated in the bridge when it was constructed in 1996. Each isolator has a total height of 0.30 m, composed of 16 steel shim plates, 17 rubber layers with a total thickness of 204 mm, and two 25 mm thick end plates (Figure 3b). A group of 4 bearings, resting on the cap beam of each of the 7 piers and on the stem wall of each of the 2 abutments, connects the 4 steel girders with the pier columns and abutments, respectively. The section size of the HDRBs located at the SA, pier columns (P#1-P#7), and North abutment is 0.50 × 0.50, 0.85 × 0.55, and 0.70 × 0.50 m, respectively. More information about the mechanical properties of the seismic isolators will be presented in Section 4.1, and detailed information about the rubber properties can be found in Boroschek et al.[17]

2.3 | Recorded earthquake response

On February 27, 2010, the Marga-Marga Bridge was subjected to the Mw 8.8 Maule, Chile earthquake. The bridge was located about 400 and 270 km from the epicenter and main asperity of the earthquake, respectively. No damage was observed on the bridge, while damage to other civil structures was substantial (eg, other studies[6,18]). The monitoring system worked properly during the earthquake; all sensors except the triaxial accelerometer located in the free field near the SA (channels 22-24) were triggered, and they recorded the bridge response and free-field ground motion in the valley. The 3 components of ground motion acceleration recorded at the free-field station in the valley are shown in Figure 4. Peak ground accelerations of 0.35g, 0.26g, and 0.34g were recorded in the longitudinal, vertical, and transverse directions, respectively. In contrast, the peak accelerations of the bridge deck recorded over pier P#4 were 0.18g, 0.31g, and 0.58g, in the longitudinal, vertical, and transverse directions, respectively. It is noted that the raw acceleration time histories were detrended and filtered using a band-pass IIR Butterworth filter of order 4 with cutoff frequencies at 0.15 and 30 Hz and that the displacement time histories were obtained through double integration of the processed acceleration time histories.

The dynamic response of the bridge recorded during the earthquake is also investigated (see Figures 5 and 6). Figure 5 shows the deformation time histories of the seismic isolators over pier P#4 as well as the deformation orbit. The isolator deformation was computed from the absolute displacement time histories obtained by double integration of the recorded deck accelerations (ie, channels 7 and 9) and pier top accelerations (ie, channels 4 and 6) in the longitudinal and transverse directions of

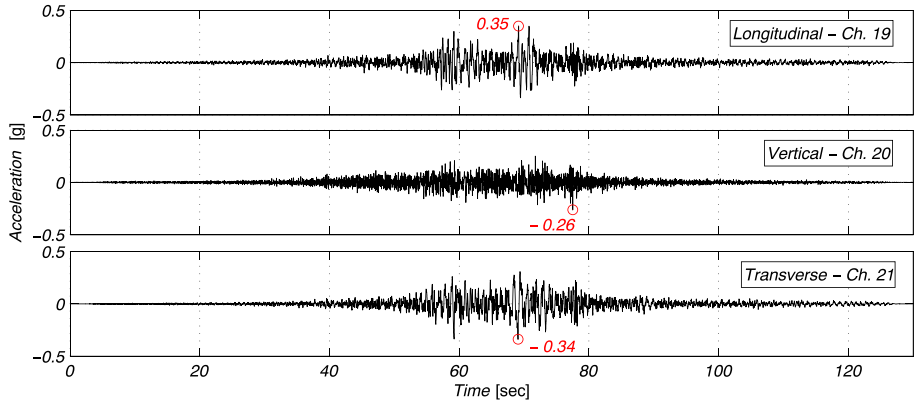

FIGURE 4 Free-field earthquake ground acceleration time histories recorded in the valley [Colour figure can be viewed at wileyonlinelibrary.com]

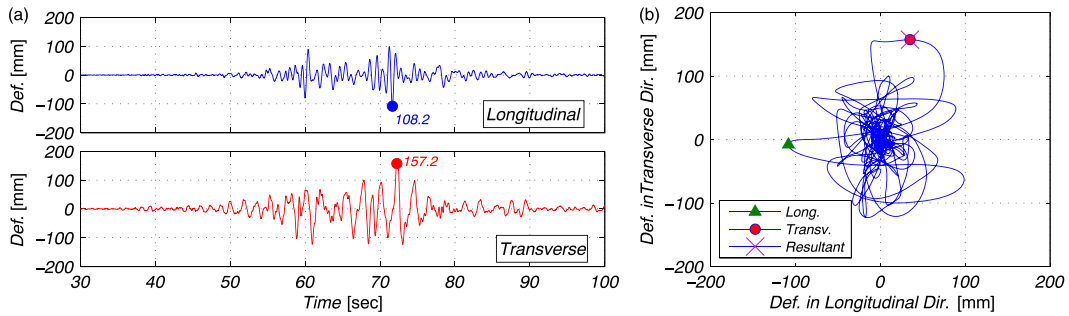

FIGURE 5 Deformation of the seismic isolators over pier P#4: (a) longitudinal and transverse deformation time histories, and (b) deformation orbit [Colour figure can be viewed at wileyonlinelibrary.com]

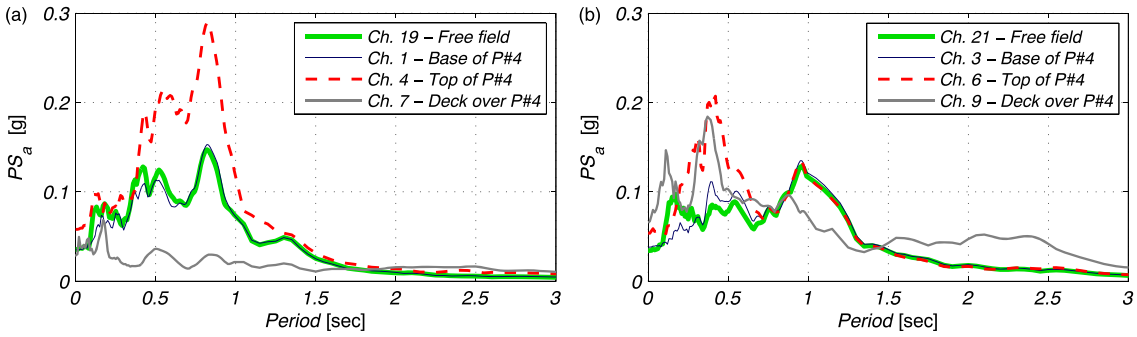

FIGURE 6 Elastic pseudo-acceleration response spectra (PS_a) ($\xi = 5\%$) for representative recorded horizontal acceleration time histories: (a) longitudinal direction, and (b) transverse direction [Colour figure can be viewed at wileyonlinelibrary.com]

the bridge. The peak deformation of the isolators over pier P#4 is 108.2 and 157.2 mm in the transverse and longitudinal directions, respectively (see Figure 5a). The peak resultant lateral deformation of 162.0 mm in the radial direction occurred at the same instant as the peak deformation in the transverse direction (see Figure 5b).

Figure 6 shows the 5% damped elastic pseudo-acceleration response spectra of representative recorded horizontal accelerations. Soil-structure interaction (SSI) effects can be observed by comparing the elastic pseudo-acceleration response spectra of the horizontal ground motions recorded at the free field in the valley to those recorded at the base of pier P#4. For each horizontal component, the spectral ordinates at the free field (channels 19 and 21) and at the base of pier P#4 (channels 1 and 3) are similar for periods longer than 0.7 second, but noticeable differences are observed in the period range below 0.7 second. In this paper, the ground acceleration recorded at the base of pier P#4 is used as seismic input excitation for all the piers, ie, rigid base condition is assumed at the base of all piers. Thus, SSI effects are accounted for, except for the rotations at the base of the piers. The effects of the seismic isolation are also clearly observed by comparing the elastic pseudo-acceleration response spectra in the longitudinal and transverse directions at the top of pier P#4 (channels 4 and 6, respectively) to those at the deck over pier

P#4 (ie, channels 7 and 9, respectively). The reduction of most of the spectral ordinates at short periods, due to the seismic isolation induced elongation of the predominant vibration periods of the bridge, demonstrates the proper behavior and significant role of the isolation system during the earthquake. Such isolation effects can also be observed from the comparison of amplitudes of the estimated transfer functions between the acceleration time histories recorded on the bridge (deck and pier top) and the ground motions recorded at the base of pier P#4.[19]

3 | FE MODEL, COMPUTING PLATFORM, AND PREDICTION ERROR

3.1 | FE model

Analytical computational models are often used for response prediction and performance assessment of large and complex civil structures. Herein, a detailed three-dimensional (3-D) nonlinear FE model of the Marga-Marga Bridge is developed in OpenSees to simulate the bridge response to the 2010 Maule earthquake. The bridge superstructure was designed as a capacity protected component to behave quasi-linear elastically. Therefore, the 4 steel girders and the RC deck, assumed to behave monolithically, are modeled using 18 linear elastic beam-column elements per span, with composite steel-concrete section properties calculated from the geometric dimensions specified in the blueprints of the bridge and using an elastic modulus of 210 GPa for the steel girders and 23.5 GPa for the concrete deck. A series of fictitious rigid beam-column elements (exceedingly stiff) are used to model the (assumed) rigid offsets between the centroidal axes of the steel girders and that of the RC deck (see Figure 7a).

Each bridge pier column is modeled using 5 or 6 (depending on the height) displacement-based nonlinear fiber-section beam-column elements with 7 Gauss-Lobatto integration points along the length of each element. The pier cross sections are discretized into fibers, and uniaxial realistic material constitutive models are assigned to each of the concrete and steel fibers of each pier cross section. The OpenSees *concrete01* material model and *concrete02* material model are used for the unconfined concrete cover layer and the confined concrete core, respectively. The OpenSees *steel02* material model is used to model the reinforcing steel (ie, longitudinal reinforcing bars). The pier cap beam is modeled using quasi-rigid beam-column elements to represent the part over the pier top and 2 nonlinear beam-column elements to represent each of the cantilever parts (see Figure 7a). A suite of rigid beams, modeled by linear elastic beam-column elements with exceedingly stiff (quasi-rigid) properties, are used to represent various geometric offsets in the model.

Each HDRB seismic isolator is modeled using an elastomeric bearing element, referred to as the Elastomeric Bearing (Plasticity) Element, in OpenSees. This is a plasticity-based (rate-independent) phenomenological model to describe the coupled bidirectional shear force-deformation response of seismic isolators. Nonlinear hardening effects can also be captured by the model through the parameters α and μ (see Figure 7b).

The inertial (mass) properties of the bridge structure are calculated based on the mass density of the structural materials and the volume of structural components and are lumped at the nodes of the FE model. Only the 3 translational mass components are considered. The mass- and initial stiffness–proportional Rayleigh damping model with a critical damping ratio of 2% assigned at the first transverse and longitudinal modes of the bridge is used to represent the sources of energy dissipation

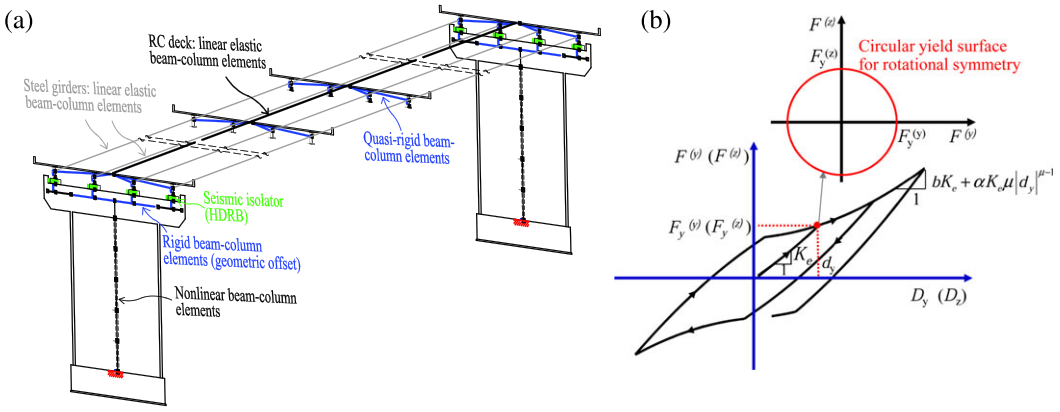

FIGURE 7 Schematic view of the FE model for the bridge: (a) a single span, and (b) the lateral force-deformation response behavior used to model the seismic isolators. FE, finite element; RC, reinforced concrete [Colour figure can be viewed at wileyonlinelibrary.com]

beyond the energy dissipated through inelastic actions of the materials and seismic isolators. To avoid the introduction of artificial viscous damping in the isolation system, the bearing elements are specified to not contribute to the Rayleigh damping model defined for the overall bridge structure.

The FE model of the bridge considered in this paper does not explicitly model the abutments because the motions at the bridge ends (channels 11, 12, 17, and 18) were recorded and are imposed as part of the seismic input for seismic response simulation. Furthermore, the ground motion recorded at the base of pier P#4 (channels 1 to 3) is assumed as the input excitation at the base of all piers, ie, rigid base condition is assumed at the base of all piers. The vertical base excitation is assumed to be uniform over the entire bridge system, ie, the vertical acceleration recorded at the base of pier P#4 (channel 2) is also used as the vertical excitation at the bridge ends. Therefore, multiple-support excitation is used for the seismic response simulation of the bridge, yet neglecting the rotational base excitations due to SSI.

3.2 | Cloud-based high-throughput distributed computing

In nonlinear FEMU, optimization aims to minimize the discrepancy between the measured and FE-predicted responses. In this paper, a sophisticated optimization method (ie, sequential quadratic programming) is used first for the calibration of isolator models based on component test data. Additionally, a grid-based optimization approach is used for both the component-level and system-level FEMU problems, which are treated as high-throughput problems like those related to sensitivity analysis or Monte Carlo simulation using computationally intensive models. This type of problems involves a large number of parameter sets (to cover the feasible domain of the parameters) and thus a large number of independent simulation jobs to be run. With the ever-growing computing power and the cloud computing resources available through workflow management systems such as *HTCondor* and *GlidinWMS*,[20] brute-force optimization is a feasible approach for FEMU problems, since many independent jobs can run concurrently in a cluster of processors on the cloud. Therefore, brute-force optimization making use of high-throughput cloud computing offers an attractive alternative to other optimization methods (eg, gradient-based and pattern search optimization algorithms), which cannot make full use of available computing resources to evaluate a large number of functions (models) simultaneously. In this study, the computational work was performed using the computational resources of the Open Science Grid cluster at the University of California, San Diego, accessed via workflow management system *GlideinWMS*.

3.3 | Goodness-of-fit metrics for bridge response time histories

Two goodness-of-fit (GOF) metrics are defined to quantify the prediction error, ie, the discrepancy between the recorded and FE-predicted response time histories of the bridge. The first GOF metric is the root-mean-square error (*RMSE*) of the difference between the time series $r_k^{i,\ recorded}$ and $r_k^{i,\ predicted}$, as defined in Equation 1. Here, r denotes the type of response of interest (eg, displacement), the superscript i indicates the specific response record (eg, acceleration response measured at a channel), the subscript k designates the time step or discrete time t_k at which the response is measured or predicted, and N_t is the total number of data samples considered within a time window (eg, 40-100 seconds). The second GOF metric is the relative RMSE (*RRMSE*), which is a normalized version of the *RMSE*, as defined in Equation 2. In this case, the GOF metric is normalized by the root-mean-square of the corresponding recorded response. Note that both GOF metrics are equivalent when the FE model is tuned to have a good fit for only one response record of interest. When multiple response records are considered for the FEMU, the *RRMSE* metric automatically accounts (ie, normalizes) for the different magnitudes of the various response records considered in a multiobjective optimization problem (ie, the *RRMSE* metric attributes the same weight to response records of different magnitudes).

$$RMSE\left(r^i\right) = \sqrt{1/Nt\sum_{k=1}^{N_t}\left(r_k^{i,\ recorded} - r_k^{i,\ predicted}\right)^2} \tag{1}$$

$$RRMSE\left(r^i\right)[\%] = \sqrt{\left[1/N_t\sum_{k=1}^{N_t}\left(r_k^{i,\ recorded} - r_k^{i,\ predicted}\right)^2\right]} \Big/ \sqrt{\left[1/N_t\sum_{k=1}^{N_t}\left(r_k^{i,\ recorded}\right)^2\right]} \times 100 \tag{2}$$

4 | TWO-PHASE FEMU

Due to the high computational cost for simulating the complete bridge response for the long-duration earthquake excitation considered here, tuning a large number of model parameters (eg, parameters associated to the isolator model, the boundary conditions at the abutments, concrete/steel materials, and the damping model) simultaneously is a very challenging task. More

importantly, considering an excessive number of parameters may induce overfitting and, consequently, incorrect estimation of dominant sensitive parameters (curse of dimensionality). To focus the estimation on the model parameters of the seismic isolators, a 2-phase FEMU process is conducted on the bridge system excluding the abutments (ie, without explicit modeling of the abutments) by imposing the recorded motions at the bridge ends. This allows this study to focus on the isolators on top of the pier columns. Note that the rotational behavior (about a vertical axis) of the bridge at the bridge ends is assumed to be restrained by the abutments and the torsional stiffness provided by the seismic isolator bearings.

The seismic isolator model is first calibrated with experimental data collected from component tests conducted on prototypes of the HDRBs installed in the bridge.[17] This calibration is performed by minimizing the mean square error between the component test data and the numerical model using a gradient-based optimization tool, OpenSees-SNOPT,[21] as well as a grid-based brute-force optimization approach (ie, through a parametric analysis). This optimization problem is referred to herein as phase I FEMU. The updated seismic isolator model will then be used in the bridge model to evaluate the GOF between the measured and FE-predicted bridge responses. Phase I will help define a feasible domain in the seismic isolator parameter space that will be very useful during Phase II when the measured response of the bridge during the 2010 Maule earthquake will be used to update the estimate of the seismic isolator parameters of the nonlinear FE model of the bridge.

4.1 | Phase I: isolator model calibration based on component test data

In this section, the experimental data available from 23 tests, conducted under different loading protocols on the 0.85×0.55 m isolator specimens,[17] are used to estimate the model parameters of the seismic isolators on top of the bridge piers. Note that the seismic isolators on abutment stem walls are not included in the FE model since recorded bridge end motions are imposed. In this phase of component-wise FEMU for the seismic isolator, a single degree of freedom model is defined in OpenSees using an elastomeric bearing element and subjected to the displacement loading histories from the loading protocols. For each set of experimental data, nonlinear least square optimization is performed to minimize the discrepancy between the FE-predicted and recorded lateral force histories, $F_{\text{model}}(d_i;\boldsymbol{\theta})$ and $F_{\text{exp}}(d_i)$, respectively. The optimization problem is mathematically formulated as

$$\min_{\boldsymbol{\theta}} \left\{ \sqrt{\sum_{i=1}^{\#\ \text{of data points}} \left[F_{\text{model}}(d_i;\boldsymbol{\theta}) - F_{\text{exp}}(d_i)\right]^2} \right\} \quad \textit{subjected to} \quad \boldsymbol{\theta}^l \le \boldsymbol{\theta} \le \boldsymbol{\theta}^u \tag{3}$$

where d_i is the lateral deformation of the isolator specimen at discrete time t_i during the loading history and $\boldsymbol{\theta}$ represents the isolator model parameter vector. The lower and upper bounds of $\boldsymbol{\theta}$, denoted as $\boldsymbol{\theta}^l$ and $\boldsymbol{\theta}^u$, respectively, are specified later for various optimization problems. The seismic isolator model used (see Figure 7b) is governed by 5 parameters, ie, $\boldsymbol{\theta} = [F_y,\ K_e,\ b,\ \alpha,\ \mu]$, in which F_y is the yield strength, K_e is the initial stiffness, b is the postyield to preyield stiffness ratio, and α and μ are parameters characterizing the shape of the nonlinear hardening branch of the force-deformation curve.

Nonlinear hardening is most likely to occur when a HDRB is subjected to large lateral deformations. Therefore, the seismic isolator specimen that reached the largest shear strain (106% or 216 mm of lateral deformation) during the component tests (eg, VD20C3) is first analyzed to detect possible nonlinear hardening effects. Two optimization problems, one including and the other excluding parameters α and μ, are formulated and solved. In the first optimization problem, the model parameter vector $\boldsymbol{\theta} = [F_y,\ K_e,\ b,\ \alpha,\ \mu]$ with lower bound $\boldsymbol{\theta}^l = [4.5 \times 10^{-3}$ kN, 1.0×10^{-4} kN/mm, 0.0, −2.0, 0.0] and upper bound $\boldsymbol{\theta}^u = [1.0 \times 10^{20}$ kN, 1.0×10^{20} kN/mm, 1.0, 2.0, 3.0] is considered. The second optimization problem considers the model parameter vector $\boldsymbol{\theta} = [F_y,\ K_e,\ b]$, and the nonlinear hardening term is eliminated by setting $\alpha = 0$ and $\mu = 1.0$ (see Figure 7 b). OpenSees-SNOPT, which resorts to a sequential quadratic programming algorithm for solving nonlinear optimization problems, is used for both optimization problems. The optimization results are shown in Figure 8 for the cases with and without nonlinear hardening. The optimization algorithm drives the initial isolator model parameters (defining the starting model), which fit the experimental results poorly, towards the optimized isolator model parameters (defining the optimum model), which fit the experimental results very well. It is observed from Figure 8 that the inclusion of the nonlinear strain hardening parameters α and μ barely improves the fit with the experimental data. Thus, it is concluded that a simplified version of the elastomeric bearing model, with linear hardening only, is appropriate to simulate the behavior of the seismic isolators during the component tests (maximum lateral deformation of 216 mm) for the isolator prototypes and during the 2010 Maule earthquake (maximum lateral deformation of about 162 mm, see Figure 5b) for the Marga-Marga Bridge. This leads to a relatively low-dimensional parameter space, thus all the model parameter estimation problems later in this paper are to determine the optimal isolator model parameter vector $\boldsymbol{\theta}^* = \left[F_y^*,\ K_e^*,\ b^*\right]$.

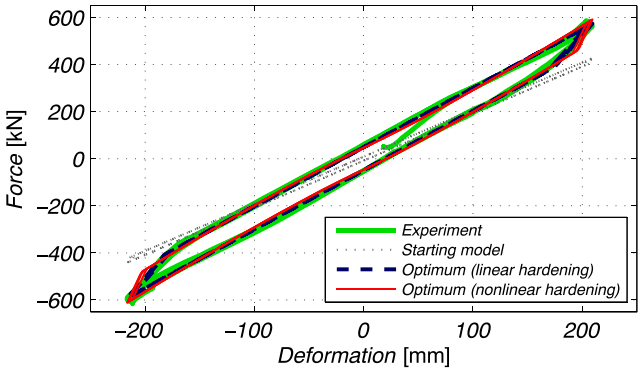

FIGURE 8 Calibration of isolator model parameters using component test data VD20C3 to explore the nonlinear hardening branch [Colour figure can be viewed at wileyonlinelibrary.com]

For each component test, an elastomeric bearing model with parameter vector $\boldsymbol{\theta}=[F_y,\ K_e,\ b]$ is updated by fitting the model to the experimentally determined force-deformation hysteretic response. The optimization problems formulated with the design variable vector $\boldsymbol{\theta}=[F_y,\ K_e,\ b]$ are solved using both OpenSees-SNOPT and the grid-based brute-force approach. When using OpenSees-SNOPT, different starting points ($\boldsymbol{\theta}^0$) can be considered since this gradient-based algorithm can lead to local minima, thus 2 different starting points (ie, $\boldsymbol{\theta}_1^0=[45.0\text{kN},\ 10.5\text{kN/mm},\ 0.19]$ and $\boldsymbol{\theta}_2^0=[30.0\text{kN},\ 2.8\text{kN/mm},\ 0.50]$) are used. For the grid-based optimization approach, a parameter search space is defined by $F_y\in[5.0,\ 100.0]$ kN, $K_e\in[5.55,\ 30.55]$ kN/mm, $b\in[0.15,\ 0.80]$ based on the optimal parameter sets obtained using OpenSees-SNOPT, and a grid of $12\times12\times10$ uniform mesh is used. The 3 sets of optimal solutions are plotted in Figure 9, which illustrates the local optimality issue, ie, possible deviations of the optimum results obtained using the gradient-based optimization tool OpenSees-SNOPT from those obtained using the grid-based brute-force approach.

Figure 9a shows the optimal isolator model parameters for the 23 tests conducted on 0.85×0.55 m isolator prototypes. For the objective function quantifying the discrepancy between the FE-predicted and experimental lateral force history, a gradient-based approach can easily be trapped into a local minimum, which highly depends on the starting point. This is clearly evidenced by the fact that only a few optimum solutions from the gradient-based approach are close to those from the grid-based brute-force approach. The optimal isolator model parameters obtained from the 23 data sets exhibit a large scatter (Figure 9a), partly because of differences in the loading protocols (eg, maximum deformation and loading speed). However, the least-square fitted postyield stiffness bK_e, plotted in Figure 9b against the maximum experimental shear strain, shows little scatter between $\boldsymbol{\theta}^*$, $\boldsymbol{\theta}_1^*$, and $\boldsymbol{\theta}_2^*$ for most cases, especially those with large-yield excursions (ie, shear strain ≥50%). Note that the postyield stiffness bK_e is a very important parameter that needs to be well calibrated.

To further compare the optimum isolator model parameters obtained through gradient-based optimization (with both starting points) and the grid-based brute-force approach, the color-coded objective function (see Equation 3) for an

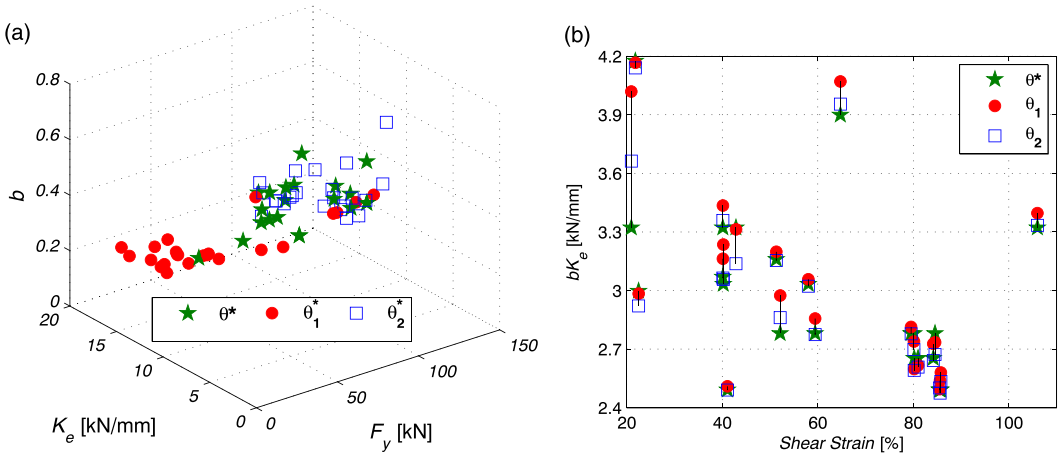

FIGURE 9 Optimal isolator model parameter sets obtained from the component test data: (a) all parameter sets, and (b) postyield stiffness bK_e versus maximum experimental shear strain [Colour figure can be viewed at wileyonlinelibrary.com]

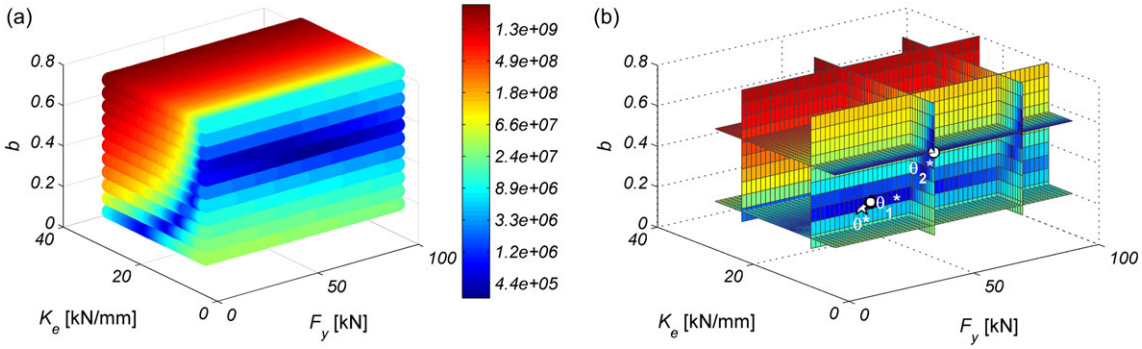

FIGURE 10 Color-coded objective function to be minimized for the isolator component test V22015: (a) 4-D plot, and (b) volumetric slice plot [Colour figure can be viewed at wileyonlinelibrary.com]

isolator component test (eg, V22015) is shown in Figure 10. Figure 10a provides a comprehensive view of the topology of the objective function, which shows that the value of the objective function (as the fourth dimension indicated by color) varies widely over the 3-D parameter search space. Figure 10b shows a volumetric slice plot of the 4-D plot, providing an inside view of the objective function as well as the location of the optimum design points for the gradient-based approach with 2 starting points ($\boldsymbol{\theta}_1^*$ and $\boldsymbol{\theta}_2^*$) and for the grid-based brute-force approach ($\boldsymbol{\theta}^*$). The optimum design point $\boldsymbol{\theta}_2^*$ is found to be a local minimum located relatively far from the global minimum $\boldsymbol{\theta}^*$, while $\boldsymbol{\theta}_1^*$ approximately coincides with $\boldsymbol{\theta}^*$. In view of the local optimality issues encountered for calibration of the isolator model, grid-based brute-force optimization proves to be a more appropriate and robust approach than gradient-based optimization, especially when cloud-based high-throughput computing can be used for optimization problems with a low dimension.

The optimal isolator model parameters obtained from the grid-based brute-force approach are used in the bridge model to simulate its response to the 2010 Maule earthquake. It is noted that in the bridge model, the seismic isolators located between the piers and the bridge superstructure are of uniform size (0.85×0.55 m). Because of the bridge configuration, a similar level of deformation in the longitudinal direction is expected for all the isolators, while different levels of deformation are anticipated in the transverse direction. However, it is impractical to have an isolator model with maximum deformation-dependent parameters, ie, using different isolator models for the various seismic isolators installed in the bridge. Thus, the isolator model with a unique set of model parameters is used for all elastomeric isolators over the pier columns in the bridge, an assumption commonly used in research and engineering practice.

The accuracy of the isolator model parameters calibrated from the isolator component test data is evaluated in terms of GOF metrics defined in Equation 2 for the bridge response to the 2010 Maule earthquake. Table 1 reports the *RRMSE* between the measured responses and the corresponding FE-predicted responses based on the bridge model using the optimum isolator model parameters ($\boldsymbol{\theta}^*$), which are obtained from the individual component test data and the brute-force approach. These response quantities are the absolute displacement response time history at the top of pier P#4 in the longitudinal and transverse directions, $U_{P\,\#4}^{Long.}$ and $U_{P\,\#4}^{Transv.}$; the absolute displacement response of the bridge deck over pier P#4 in the longitudinal and transverse directions, $U_{Deck\ over\ P\,\#4}^{Long.}$ and $U_{Deck\ over\ P\,\#4}^{Transv.}$; and the absolute displacement of the bridge deck over pier P#2 in the transverse direction, $U_{Deck\ over\ P\,\#2}^{Transv.}$. It is observed that the optimal isolator model parameter set obtained from component test VDL19C provides the best fit of the longitudinal displacement response $U_{P\,\#4}^{Long.}$ among all 23 component tests; whereas the optimal model parameter set obtained from component test VE140 results in the best fit of the transverse displacement responses $U_{P\,\#4}^{Transv.}$, $U_{Deck\ over\ P\,\#4}^{Transv.}$, and $U_{Deck\ over\ P\,\#2}^{Transv.}$. However, none of the optimum model parameter sets obtained from the individual component test data provide the best fit of the displacement responses in both the longitudinal and transverse directions. The optimal isolator model parameter set that best fits the bridge response in the longitudinal (transverse) direction is obtained from component test VDL19C (VE140) with peak deformation of 173 mm (175 mm), which is larger than the peak longitudinal (transverse) deformation of the elastomeric isolator on top of pier P#4 during the 2010 Maule earthquake, ie, 108.2 mm (157.2 mm). It is observed that the measured responses of the bridge are predicted better when using optimum isolator model parameters obtained from component tests with large maximum deformations, but this does not guarantee the best FE prediction of the bridge response, because of the large variability observed in the optimal isolator model parameter sets (see Figure 9) as well as in the corresponding *RRMSE*s (see Table 1). This calls for the calibration of the isolator model using the recorded response of the bridge to the 2010 Maule earthquake.

TABLE 1 *RRMSE* between measured response and FE-predicted response based on the bridge model using optimum isolator model parameter sets ($\boldsymbol{\theta}^*$) obtained from individual component test data and grid-based brute-force approach

Component Test ID	Peak Deformation, mm	RRMSE, %				
		$U^{Long.}_{P\ \#4}$ (Ch. 4)	$U^{Transv.}_{P\ \#4}$ (Ch. 6)	$U^{Transv.}_{Deck\ \ over\ \ P\ \#4}$ (Ch. 9)	$U^{Long.}_{Deck\ \ over\ \ P\ \#4}$ (Ch. 7)	$U^{Transv.}_{Deck\ \ over\ \ P\ \#2}$ (Ch. 13)
V22011	44.5	56.29	26.97	134.00	6.27	114.74
V22012	43	46.86	18.05	81.51	6.07	74.07
V22013	82	42.95	18.93	98.41	6.02	85.59
V22014	82	40.72	15.92	67.76	**5.99**	64.25
V22015	105	37.51	16.24	77.59	6.00	70.74
V22016	106	37.70	14.76	53.73	6.01	54.95
V22017	118	38.11	16.78	86.09	6.52	78.18
V22018	121	35.77	14.69	55.74	**5.99**	55.98
V22019	162	31.18	15.57	75.48	6.03	68.35
V220110A	165	35.47	14.26	46.31	6.04	50.28
V220110B	164	35.47	14.26	46.31	6.04	50.28
V220111	175	34.58	14.21	45.87	6.05	50.10
V220112	172	34.67	14.45	52.67	**5.99**	53.87
V220113	164	29.90	16.12	86.69	6.06	75.47
V220114	82	37.51	16.24	77.59	6.00	70.74
VD12C3	132	300.25	21.03	214.29	7.31	177.26
VD20C3	216	32.08	14.10	48.00	6.02	50.92
VD4C3	46	52.81	29.00	157.15	6.00	130.26
VD8C3	84	42.87	19.29	102.77	6.03	88.71
VF20C	88	43.08	19.66	106.68	6.04	91.56
VDL19C	173	**29.05**	15.38	76.00	6.02	68.06
VE140	175	34.84	**13.20**	**40.78**	6.12	**46.54**
VE304	175	34.58	14.21	45.87	6.05	50.10

Abbreviations: FE, finite element; RRMSE, relative root-mean-square error.

4.2 | Phase II: isolator model calibration based on recorded seismic bridge response data

In this section, a bridge system model with the abutments excluded (by imposing motions at the bridge ends as recorded), as defined in Section 3.1, is used to estimate the isolator model parameters. The bridge displacement responses (obtained through double integration of the recorded acceleration responses) at the bridge superstructure and at the top of pier columns P#4 and P#2, in both the longitudinal and transverse directions, are used to estimate the isolator model parameters (ie, K_e, F_y, and b). Optimization problems considering single or multiple objective function(s) are formulated and solved using the grid-based brute-force approach by taking advantage of cloud-based high-throughput distributed computing capabilities. The 3-D search domain for the 3 isolator parameters is the same as that used for the isolator model calibration based on the component tests. This grid-based optimization task requires to run 1440 jobs of seismic response simulation of the bridge subjected to the 2010 Maule earthquake with a long duration (ie, 130 seconds). If performed on a desktop computer, this computational optimization task would require approximately 2.0 years, since each seismic response simulation consumes 13.0 hours of computational time on a local desktop computer (Intel Core i7 CPU, 2.80 GHz, 8.0 GB RAM). However, it took less than 24 hours (wall clock time) to complete all these jobs using high-throughput computing on the platform defined earlier, since approximately 800 jobs were run simultaneously.

In the optimization problem, various recorded bridge response quantities (eg, $U^{Long.}_{P\ \#4}$, $U^{Long.}_{Deck\ \ over\ \ P\ \#4}$, $U^{Transv.}_{P\ \#4}$, $U^{Transv.}_{Deck\ \ over\ \ P\ \#4}$, and $U^{Transv.}_{Deck\ \ over\ \ P\ \#2}$) can be used in defining the GOF as the objective function to seek for the optimum values of the seismic isolator model parameters. The GOF metrics $RMSE_i$ and $RRMSE_i$ (see Equations 1 and 2), with response index $i = 1, 2, 3,$

4, and 5 for $U^{Long.}_{P\ \#4}$, $U^{Long.}_{Deck\ \ over\ \ P\ \#4}$, $U^{Transv.}_{P\ \#4}$, $U^{Transv.}_{Deck\ \ over\ \ P\ \#4}$, and $U^{Transv.}_{Deck\ \ over\ \ P\ \#2}$, respectively, will be used in the objective function(s) of the single-objective and multiobjective optimization problems formulated for nonlinear FEMU in this section.

To classify and compare different objective functions, the concepts of conflicting (or competing) objectives (ie, objectives compete with each other and thus attain their minima at different design points in the parameter space), consistent objectives (ie, objectives share common trends and attain their minima at approximately the same design point in the parameter space), and neutral objectives (ie, objectives tend to be flat and do not vary significantly over the parameter space) are used. Comparison between different objective functions will be useful during the decision-making process for selecting objectives to be used in the formulation of multiobjective optimization problems. In this paper, single-objective and multiple-objective optimization setups are used for nonlinear FEMU of the bridge.

4.3 | Single-objective optimization for nonlinear FEMU

The *RRMSE* values for the response quantities $U^{Long.}_{P\ \#4}$, $U^{Transv.}_{P\ \#4}$, and $U^{Transv.}_{Deck\ \ over\ \ P\ \#4}$ are plotted as color coded (as the fourth dimension) in the 3-D design parameter space in Figures 11 to 13, respectively. These 4-D plots contain information regarding the 3-D parameter space (3-D grid of design points) spanned by the yield strength (F_y), elastic stiffness (K_e), and postyield to preyield stiffness ratio (b) parameters, as well as the color-coded *RRMSE* value calculated at each grid point. In each of the Figures 11 to 13, a volumetric slice plot is also presented for an inside view of the corresponding 4-D plot. Figure 11 shows the 4-D plot of the color-coded $RRMSE_1$ for $U^{Long.}_{P\ \#4}$. The *RRMSE* is greatly reduced from a maximum of about 2400% to a minimum of 20.4% while varying the isolator model parameters in the search domain. In contrast, $RRMSE_2$ for $U^{Long.}_{Deck\ \ over\ \ P\ \#4}$, which is not presented here but can be found in Li et al,[19] varies little with respect to the isolator model parameters. This is because the recorded horizontal motions at the bridge ends are imposed in the model and the longitudinal displacement of the bridge deck is negligibly affected by the seismic isolator properties due to the high axial stiffness of the bridge superstructure. Therefore, $RRMSE_2$ for $U^{Long.}_{Deck\ \ over\ \ P\ \#4}$ falls in the category of neutral objectives, since $U^{Long.}_{Deck\ \ over\ \ P\ \#4}$ is not sensitive to the isolator model parameters of the FE model. Figures 12 to 13 show $RRMSE_3$ for $U^{Transv.}_{P\ \#4}$ and $RRMSE_4$ for $U^{Transv.}_{Deck\ \ over\ \ P\ \#4}$, respectively, as a function of the isolator model parameters. Significant variation in the *RRMSE* over the isolator model parameter space is observed for both objectives, which emphasizes the importance of the proper selection of isolator model parameter values in the nonlinear FE model of the bridge to achieve reasonably accurate simulations of the recorded response quantities. Similarly, the color-coded pattern (or topology) of the 4-D plot of $RRMSE_5$ for $U^{Transv.}_{Deck\ \ over\ \ P\ \#2}$ agrees very well with that in Figure 13, indicating that the objectives for $U^{Transv.}_{Deck\ \ over\ \ P\ \#4}$ and $U^{Transv.}_{Deck\ \ over\ \ P\ \#2}$ are consistent.[19] However, they are conflicting with the objectives shown in Figures 11 to 12. Using the above 5 GOF metrics ($RRMSE_i$) as objective functions, 5 single-objective optimization problems are formulated as

$$\begin{aligned} &\min\ RRMSE_i(F_y,\ K_e,\ b) \qquad\qquad i = 1,\ \ldots,\ or\ \ 5\ \ (response\ index)\\ &\text{subject to} \quad 5.0 \le F_y \le 100.0, \quad 5.55 \le K_e \le 30.55, \quad 0.15 \le b \le 0.80. \end{aligned} \tag{4}$$

The single-objective optimization problems defined in Equation 4 are solved using the grid-based brute-force approach, which consists of evaluating the objective function at the nodes of a grid defined over the parameter space and then linearly

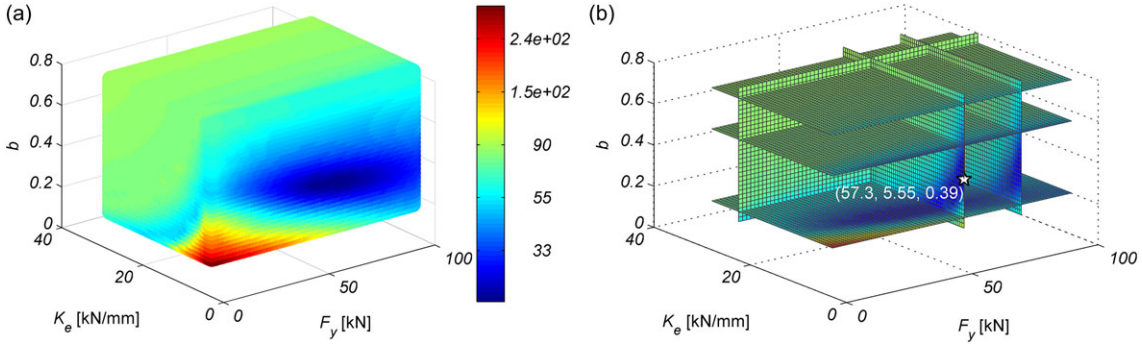

FIGURE 11 Color-coded *RRMSE* between simulated and recorded response $U^{Long.}_{P\ \#4}$ in terms of the three isolator model parameters: (a) 4-D plot, and (b) volumetric slice plot [Colour figure can be viewed at wileyonlinelibrary.com]

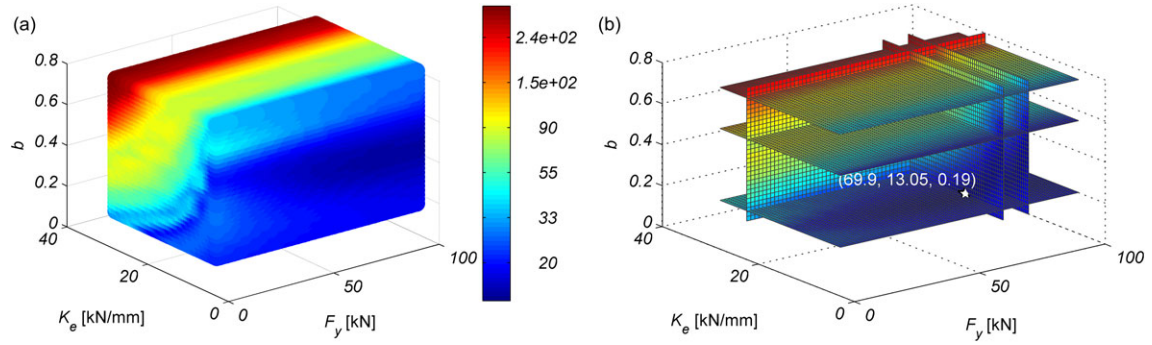

FIGURE 12 Color-coded *RRMSE* between simulated and recorded response for $U^{Transv.}_{P\ \#4}$ in terms of the three isolator model parameters: (a) 4-D plot, and (b) volumetric slice plot [Colour figure can be viewed at wileyonlinelibrary.com]

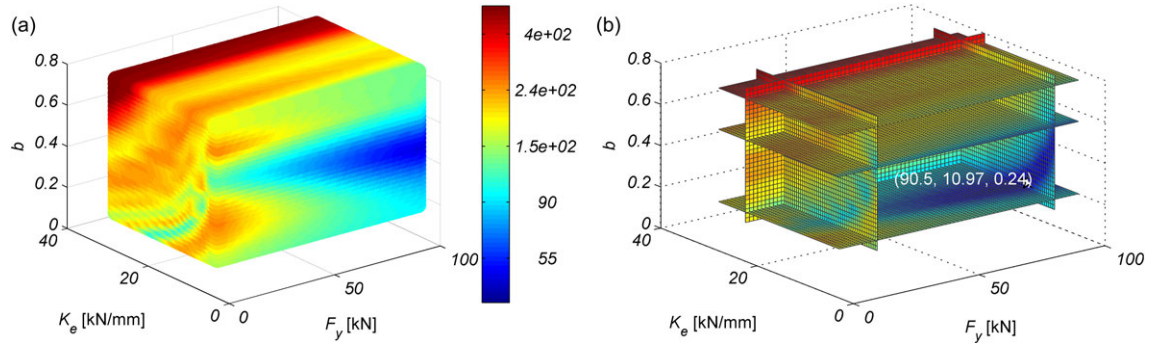

FIGURE 13 Color-coded *RRMSE* between simulated and recorded response for $U^{Transv.}_{Deck\ \ over\ \ P\ \#4}$ in terms of the 3 isolator model parameters: (a) 4-D plot, and (b) volumetric slice plot [Colour figure can be viewed at wileyonlinelibrary.com]

interpolating the objective function values in between. The optimal set of isolator model parameters obtained for each single objective function considered is marked by a white pentagram on the volumetric slice plot (in Figures 11–13).

The bridge responses simulated using the FE model with those sets of optimum isolator model parameters are presented later, after isolator model parameter estimation through multiobjective optimization is presented. The optimum sets of isolator model parameters obtained from the different single objective functions and denoted by the white pentagrams in Figures 11–13 do not coincide, implying the need for a trade-off between different response quantities. Thus, to achieve a good overall fit for all recorded response quantities, a multiobjective optimization is required.

4.4 | Multiobjective optimization for nonlinear FEMU

In this section, multiobjective optimization is used to seek an overall good fit between FE-predicted and measured response for multiple response quantities from various channels. In general, the goodness of a solution in a multiobjective optimization problem is determined by the dominance criterion, and one approach is to search for the nondominated solution set, referred to as the Pareto optimal set, in which none of the objective functions can be improved in value without degrading some of the other objective values.[22] Instead of focusing on the Pareto set, which would be a Pareto surface in a 3-D parameter space, an optimal set of isolator model parameters is obtained using the weighted sum method.[22] Weighted sum method defines an overall GOF metric as the square root of a weighted sum of squared single-objective functions with user-supplied weighting factors. Two different overall GOF metrics are considered here, one defined as the square root of the weighted average of *RRMSE*s, see Equation 5a, and the other defined as the square root of the weighted average of *RMSE*s, see Equation 5b.

$$\mathrm{F}_{\mathrm{R}}^{\mathrm{Obj}} = \overline{RRMSE} = \sqrt{\sum_{i=1}^{i=m} \gamma_i (RRMSE_i)^2}, \mathrm{F}_{A}^{\mathrm{Obj}} = \overline{RMSE} = \sqrt{\sum_{i=1}^{i=m} \gamma_i (RMSE_i)^2} \qquad (5a,b)$$

The weighting factors γ_i in the overall GOF metrics defined above are taken as binary (ie, to take the value 0 or 1) and are effectively used as flags to distinguish conflicting, consistent, and neutral objectives. In terms of the 3 types of objectives

defined above, the *RRMSE*s for $U^{Long.}_{P\ \#4}$, $U^{Transv.}_{P\ \#4}$, and $U^{Transv.}_{Deck\ \ over\ \ P\ \#4}$ (ie, $RRMSE_1$, $RRMSE_3$, and $RRMSE_4$) are identified as conflicting objectives, denoted as $F^{Obj}_1\left(U^{Long.}_{P\ \#4}\right)$, $F^{Obj}_2\left(U^{Transv.}_{P\ \#4}\right)$, and $F^{Obj}_3\left(U^{Transv.}_{Deck\ \ over\ \ P\ \#4}\right)$, respectively, and thus $\gamma_1=\gamma_3=\gamma_4=1$. If an objective (eg, $RRMSE_5$) is consistent with an objective already selected (eg, $RRMSE_4$) or is neutral (eg, $RRMSE_2$), then its weighting factor is set to 0 (ie, $\gamma_2=\gamma_5=0$), since they contribute little additional information for the multiobjective optimization problem to be solved.

Figure 14a shows the tri-objective optimization plot for nonlinear FEMU of the bridge with sampled data from FE response simulation and interpolation (of the individual GOF metrics inside the grid over the 3-D parameter space), when the *RRMSE* is used as the GOF metric for each considered response time history. The Pareto optimal front in the 3-D parameter space can be observed as the cluster of points that are not dominated by any member of the parameter space. To show more clearly the competing (antagonistic) effect between 2 objectives, Figure 14b presents a bi-objective plot, which is the projection of the tri-objective plot in Figure 14a along the $F^{Obj}_2\left(U^{Transv.}_{P\ \#4}\right)$ axis. The minimum of each objective function (single-objective GOF metric), as well as the minimum of the weighted average objective function (multiobjective overall GOF metric), are marked in Figure 14. The optimum sets of isolator model parameters obtained from single-objective and multiobjective optimization are reported in Table 2.

The accuracy of each optimal set of isolator model parameters is evaluated in terms of the GOF (ie, *RRMSE*) of each FE-predicted response time history obtained based on the bridge model using those optimal isolator model parameters. The *RRMSE*s of the FE-predicted responses relative to the corresponding recorded responses (ie, channels 4, 6, 7, 9 and 13) are reported in Table 2. When the overall GOF metric defined as the square root of the weighted average of *RRMSE*s is used as objective function (ie, $F^{Obj}_R=\overline{RRMSE}$), the optimum solution obtained coincides with that for F^{Obj}_2, see Figure 14. Therefore, the set of isolator model parameters that best fits the recorded response $U^{Transv.}_{P\ \#4}$ also yields accuracy in fitting the recorded

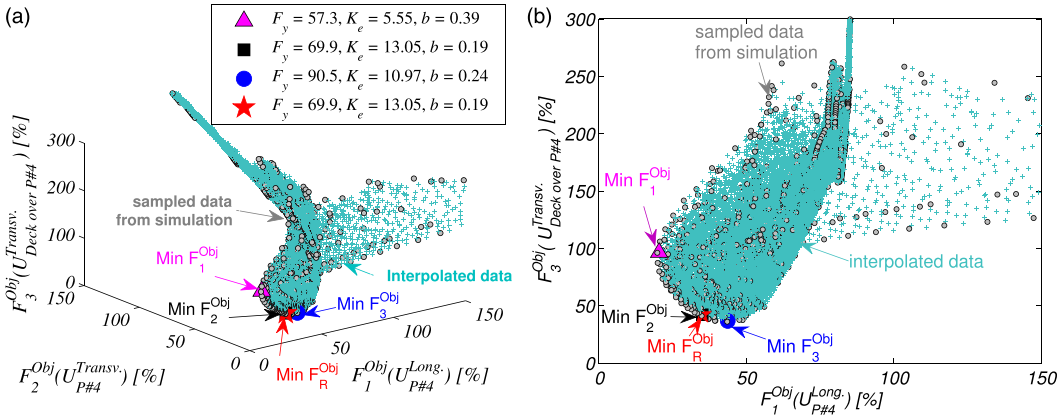

FIGURE 14 Optimization plots for nonlinear FEMU of the bridge: (a) tri-objective, and (b) bi-objective (projection of the tri-objective plot along the F^{Obj}_2 axes) [Colour figure can be viewed at wileyonlinelibrary.com]

TABLE 2 Optimum isolator model parameters obtained from single-objective and multiobjective nonlinear FEMU formulations and corresponding GOF metrics

	Optimal Isolator Model Parameters				RRMSE, %				
Obj. fn.	F_y **(kN)**	K_e **(kN/mm)**	b **(−)**	bK_e **(kN/mm)**	$U^{Long.}_{P\ \#4}$ (Ch. 4)	$U^{Transv.}_{P\ \#4}$ (Ch. 6)	$U^{Transv.}_{Deck\ \ over\ \ P\ \#4}$ (Ch. 9)	$U^{Long.}_{Deck\ \ over\ \ P\ \#4}$ (Ch. 7)	$U^{Transv.}_{Deck\ \ over\ \ P\ \#2}$ (Ch. 13)
F^{Obj}_1	57.3	5.55	0.39	2.16	20.42	15.84	96.43	6.13	82.78
F^{Obj}_2	69.9	13.05	0.19	2.48	35.10	13.16	42.12	6.27	47.47
F^{Obj}_3	90.5	10.97	0.24	2.63	43.73	13.88	36.68	6.24	45.73
F^{Obj}_R	69.9	13.05	0.19	2.48	35.10	13.16	42.12	6.27	47.47
F^{Obj}_A	90.5	10.97	0.24	2.63	43.73	13.88	36.68	6.24	45.73

Abbreviations: FEMU, finite element model updating; GOF, goodness of fit; RRMSE, relative root-mean-square error.

responses $U^{Long.}_{P\ \#4}$ and $U^{Transv.}_{Deck\ \ over\ \ P\ \#4}$. In contrast, when the overall GOF metric defined as the square root of the weighted average of *RMSE*s is used as the objective function (ie, $F^{Obj}_{A} = \overline{RMSE}$), the response quantity with the largest amplitude (ie, $U^{Transv.}_{Deck\ \ over\ \ P\ \#4}$) has dominant effect on the optimum solution. Therefore, the optimum isolator model parameters obtained in this case coincide with the optimum solution achieved by minimizing *RMSE* or *RRMSE* of $U^{Transv.}_{Deck\ \ over\ \ P\ \#4}$.

Figure 15 compares the recorded and FE-predicted response time histories obtained using the optimum isolator model parameters determined from single-objective and multiobjective optimization.

Figure 15a shows the comparison for the bridge response $U^{Long.}_{P\ \#4}$. It is observed that the best fit of the recorded time history is achieved using the optimal set of isolator model parameters obtained from the single-objective optimization for F^{Obj}_{1} ($U^{Long.}_{P\ \#4}$), reaching a *RRMSE* of 20.42%. When the optimal sets of isolator model parameters obtained from single-objective optimization using F^{Obj}_{2} and F^{Obj}_{3} are used, the *RRMSE* for $U^{Long.}_{P\ \#4}$ increases to 35.10% and 43.73%, respectively. The simulated responses based on the FE models with the optimal sets of isolator model parameters obtained using the multiobjective functions $F^{Obj}_{R} = \overline{RRMSE}$ and $F^{Obj}_{A} = \overline{RMSE}$ yield *RRMSE*s for $U^{Long.}_{P\ \#4}$ of 35.10% and 43.73%, respectively. Figure 15b,c compare the FE-predicted and recorded responses $U^{Long.}_{Deck\ \ over\ \ P\ \#4}$ and $U^{Transv.}_{P\ \#4}$, respectively. A near-perfect experimental-analytical correlation is observed for $U^{Long.}_{Deck\ \ over\ \ P\ \#4}$ for the different optimal sets of isolator model parameters, because the recorded motions at the bridge ends are imposed as boundary conditions in the FE model and the longitudinal displacement of the bridge deck is easily fitted due to the high axial stiffness of the bridge deck. Figures 15d,e compare the FE-predicted and recorded responses $U^{Transv.}_{Deck\ \ over\ \ P\ \#4}$ and $U^{Transv.}_{Deck\ \ over\ \ P\ \#2}$, respectively. A reasonably good experimental-analytical correlation is obtained for these response quantities with the FE model using the optimal sets of isolator model parameters derived from the objective functions F^{Obj}_{R} (or F^{Obj}_{2}) and F^{Obj}_{A} (or F^{Obj}_{3}), see Table 2. Overall, when all the recorded response quantities in the longitudinal and transverse directions of the bridge are considered, the optimum sets of isolator model parameters obtained by minimizing F^{Obj}_{R} (or F^{Obj}_{2}) and F^{Obj}_{A} (or F^{Obj}_{3}) are observed to both provide the best fit to the recorded bridge response.

Figure 16 compares the optimum sets of isolator model parameters obtained from component test data (in phase I) and from recorded bridge response data during the earthquake (in phase II) and the corresponding GOF metric $\overline{RRMSE}$ between the recorded and FE-predicted response time histories. Most of the isolator models with parameters fitted from component test data, an approach widely used in engineering practice, fail to provide accurate simulation of the bridge response, see Table 1. In

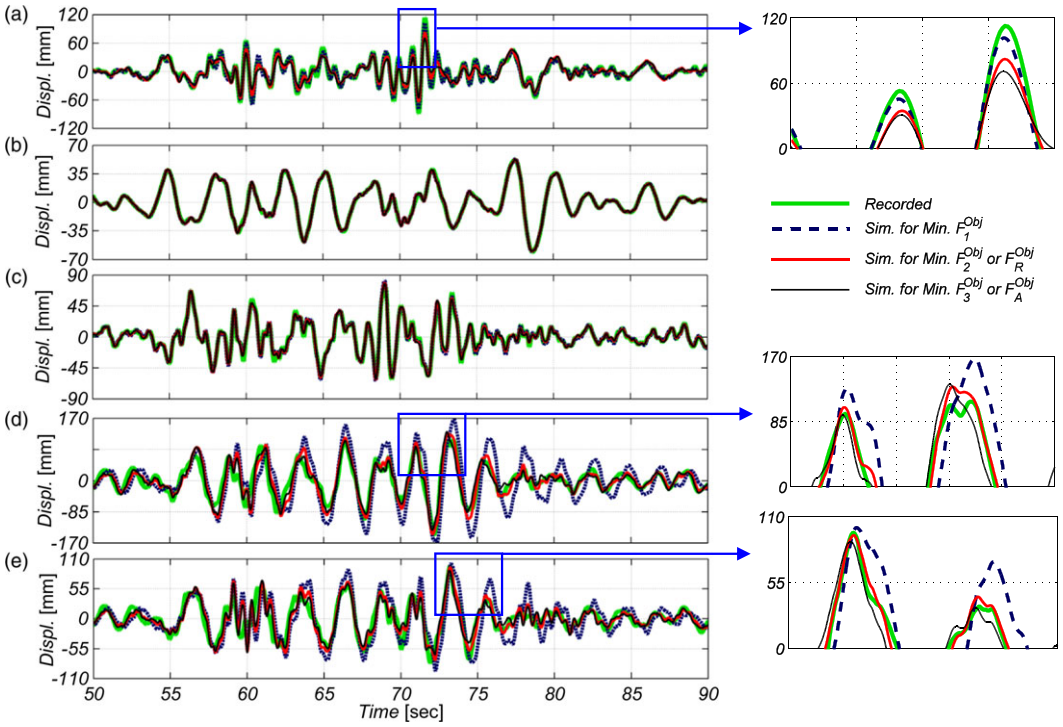

FIGURE 15 Comparison between FE-predicted and recorded responses: (a) $U^{Long.}_{P\ \#4}$, (b) $U^{Long.}_{Deck\ \ over\ \ P\ \#4}$, (c) $U^{Transv.}_{P\ \#4}$, (d) $U^{Transv.}_{Deck\ \ over\ \ P\ \#4}$, and (e) $U^{Transv.}_{Deck\ \ over\ \ P\ \#2}$. FE, finite element [Colour figure can be viewed at wileyonlinelibrary.com]

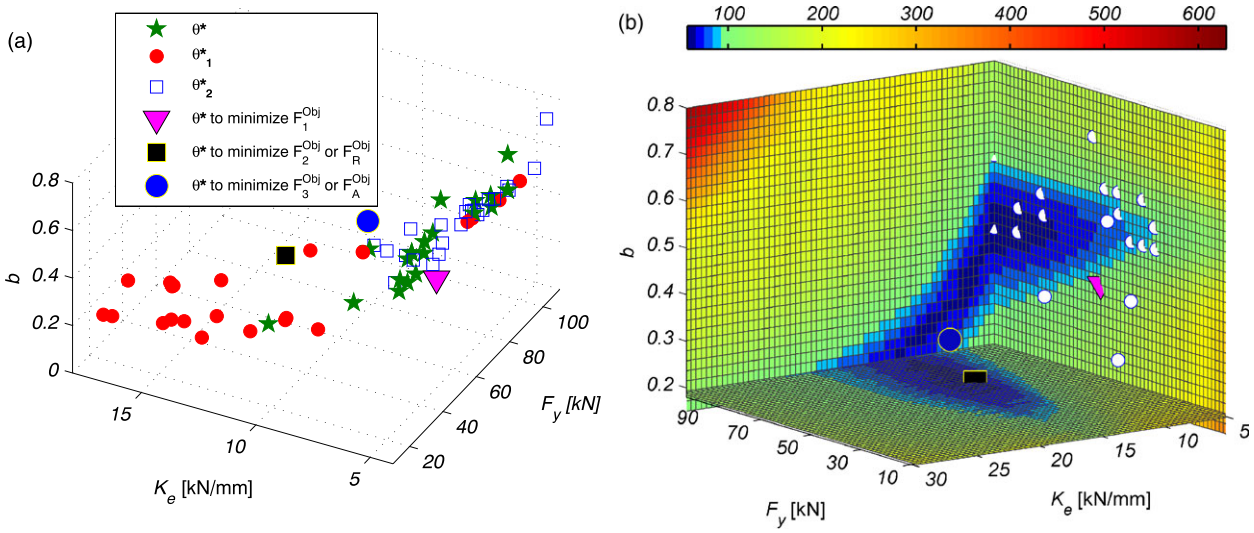

FIGURE 16 Comparison of phase I (using component test data) and phase II (using recorded bridge response data) results for isolator model calibration: (a) optimum sets of isolator model parameters, and (b) GOF metric defined as $\overline{RRMSE}$. GOF, goodness of fit [Colour figure can be viewed at wileyonlinelibrary.com]

contrast, relatively accurate FE predictions of the bridge response to the Maule earthquake are obtained when using optimal sets of isolator model parameters derived from single-objective and multiobjective optimization and the data recorded on the bridge, see Table 2.

5 | BRIDGE SEISMIC RESPONSE RECONSTRUCTION USING THE UPDATED FE MODEL

The bridge nonlinear FE model updated using a set of optimal isolator model parameters can now be used to reconstruct the seismic response of the SIB during the Maule earthquake, including the recorded and more importantly unrecorded response quantities. This provides significant insight into the effects of seismic isolation on the bridge seismic response

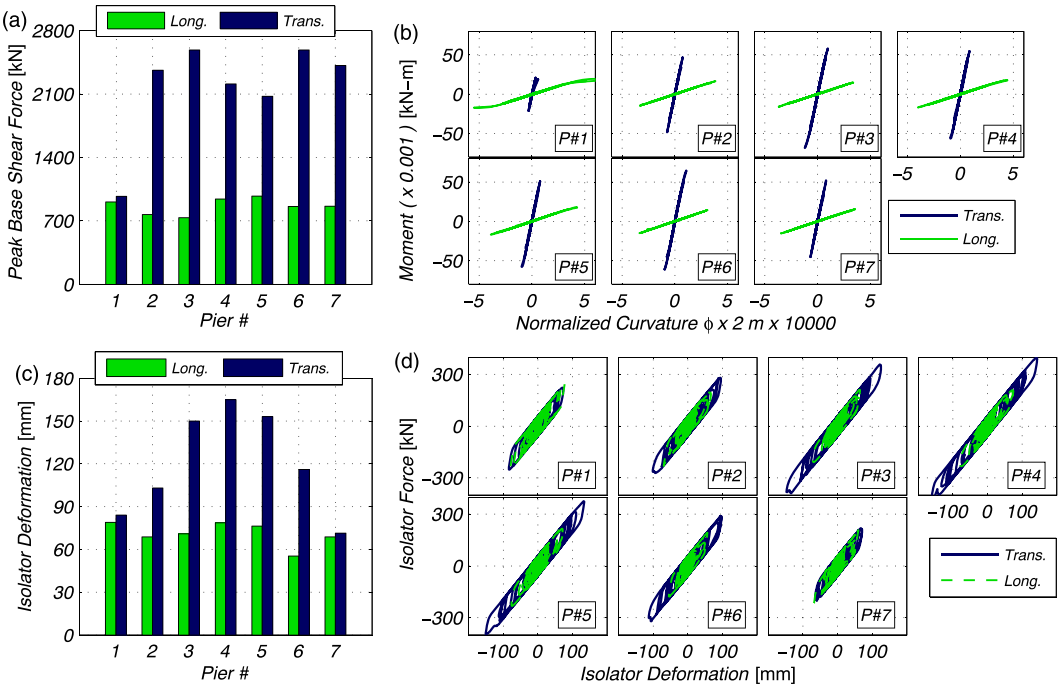

FIGURE 17 Predicted unrecorded response quantities for the 2010 Maule earthquake: (a) peak base shear forces in pier columns, (b) moment-curvature response at the base of pier columns, (c) peak deformations of seismic isolators, and (d) force-deformation response of seismic isolators [Colour figure can be viewed at wileyonlinelibrary.com]

behavior. Here, the bridge FE model with the optimal set of isolator model parameters obtained using the multiobjective function $F_R^{Obj} = \overline{RRMSE}$ is used to reconstruct the seismic response of the Marga-Marga Bridge to the 2010 Maule earthquake. Figure 17a,c show the peak base shear forces in the pier columns and peak deformations of the seismic isolators, respectively, in both the longitudinal and transverse directions. Figure 17b presents the moment-curvature response at the base of all 7 pier columns, while Figure 17d shows the force-deformation response of the seismic isolators seated on the pier columns. It is observed that the 7 pier columns remain quasi-elastic under this strong earthquake and the nonlinear behavior is concentrated in the seismic isolators. These bridge seismic response reconstruction results show that seismic isolation was very effective in mitigating and even preventing damage in the structural components of the Marga-Marga Bridge during the 2010 Maule earthquake.

6 | CONCLUSIONS

This paper focuses on nonlinear FEMU to investigate the accuracy of FE seismic response simulation of the Marga-Marga Bridge, the first seismic isolated highway bridge in Chile. The parameters of the seismic isolator model used in the nonlinear FE model of the bridge are updated (or calibrated) in 2 phases: first, based on seismic isolator component test data and second, based on the bridge response data recorded during the 2010 (Mw 8.8) Maule, Chile Earthquake.

A detailed 3-D nonlinear FE model of the bridge is developed in OpenSees for seismic response simulation. The seismic isolator model parameters are first identified through calibration with test data on seismic isolators identical to the ones in the bridge. The sets of isolator model parameters estimated from the isolator component tests exhibit a large scatter, and poor prediction/reconstruction of the bridge response to the Maule Earthquake is obtained when using the FE model with isolator parameters obtained from most of the component test data. The seismic isolator model parameters are then updated (or calibrated) using the response of the bridge recorded during the earthquake. For this purpose, single-objective and multiobjective optimization problems are formulated and solved using a grid-based brute-force optimization approach, which makes use of cloud-based high-throughput distributed computing technologies. The recorded and FE-predicted responses of the bridge are in good agreement when the optimal seismic isolator model parameters are obtained by minimizing an overall GOF metric. The FE model of the bridge updated with the set of optimal isolator model parameters is then used to reconstruct (predict) the bridge response during the earthquake, including both recorded and unrecorded response quantities. The results show that seismic isolation was effective in protecting the Marga-Marga Bridge against structural damage during the strong 2010 Maule earthquake. It is worth mentioning that no perfect solution exists for the nonlinear FEMU problem, due to aleatory uncertainties (eg, local and spatial random variabilities of material properties) and epistemic uncertainties (eg, errors/uncertainties associated with the damping model, material hysteretic models for concrete and steel, seismic isolator model, and assumptions made for the seismic input), as well as the measurement noise in the recorded data. An even better fit of the bridge recorded responses could be achieved by performing the nonlinear FEMU in a higher dimensional parameter space (including other FE model parameters such as damping) and in a probabilistic framework to account consistently for the various sources of randomness and uncertainty. It is also worth noting that the estimated isolator model parameters are not guaranteed to be optimal for predicting the response of the Marga-Marga Bridge to another earthquake. Thus, further nonlinear FEMU and validation is required to increase the confidence in the estimated parameters, for example, using the recorded bridge response data during aftershocks of the 2010 Maule earthquake.

ACKNOWLEDGEMENTS

Partial support of this research by (1) the Pacific Earthquake Engineering Research Center's Transportation Systems Research Program under award no. 1107-NCTRCJ, with Professor Steve Mahin as PEER Director and (2) the UCSD Academic Senate under research grant RN091G-CONTE is gratefully acknowledged. The first author acknowledges the support provided by the Department of Structural Engineering at UCSD through a Doctoral Dissertation Fellowship. The second author acknowledges partial support provided by the *Fondo de Ayuda a la Investigación*-UAndes and from the Chilean National Commission for Scientific and Technological Research (CONICYT), FONDECYT project no. 11160009. The authors thank Professor Maria O. Moroni and Professor Mauricio Sarrazin from the Department of Civil Engineering at the University of Chile for providing access to the data used in this study. Any opinions, findings, conclusions, or recommendations expressed in this publication are those of the authors and do not necessarily reflect the views of the sponsors.

REFERENCES

1. Akiyama M, Frangopol DM. Life-cycle design of bridges under multiple hazards: Earthquake, tsunami and continuous deterioration. *Proc., Eleventh Int. Conf. on Structural Safety and Reliability, ICOSSAR2013, Safety, and Reliability, ICOSSAR2013, Safety, reliability, risk, and life-cycle performance of structures and infrastructures*. Deodatis G, Ellingwood BR, and Frangopol DM, eds. Boca Raton, FL: CRC Press, Taylor & Francis Group; 2013:3-4.
2. Kawashima K, Unjoh S, Hoshikuma J, Kosa K. Damage of bridges due to the 2010 Maule, Chile, earthquake. *Journal of Earthquake Engineering*. 2011;15(7):1036-1068.
3. Housner G, Bergman L, Caughey T, et al. Structural control: past, present, and future. *Journal of Engineering Mechanics ASCE*. 1997;123(9):897-971.
4. Li Y, Conte JP. Effects of seismic isolation on the seismic response of a California high-speed rail prototype bridge with soil-structure and track-structure interactions. *Earthquake Engineering & Structural Dynamics*. 2016;45:2415-2434.
5. Kawashima, K. and Matsuzaki, H., 2012. Damage of road bridges by 2011 Great East Japan (Tohoku) earthquake. *15th World Conference on Earthquake Engineering*, Portugal.
6. Sarrazin M, Moroni MO, Neira C, Venegas B. Performance of bridges with seismic isolation bearings during the Maule earthquake, Chile. *Soil Dynamics and Earthquake Engineering, Special Issue dedicated to José Manuel Roësset*. 2013;47:117-131.
7. Chen MC, Pantoli E, Wang X, et al. Full-scale structural and nonstructural building system performance during earthquakes: Part I—specimen description, test protocol, and structural response. *Earthq Spectra*. 2016;32(2):737-770.
8. Mantawy, I., Thonstad, T., Sanders, D., Stanton, J., and Eberhard, M., 2014. Shake table experiments of precast, pretensioned bridge. *30th US-Japan Bridge Eng. Workshop*, Washington D.C.
9. Zhang J, Makris N. Seismic response analysis of highway overcrossings including soil–structure interaction. *Earthquake Eng & Structural Dynamics*. 2002;31(11):1967-1991.
10. Siringoringo D, Fujino Y, Namikawa K. Seismic response analyses of the Yokohama Bay cable-stayed bridge in the 2011 Great East Japan earthquake. *Journal of Bridge Engineering ASCE*. 2014;19: A4014006
11. Beck JL, Katafygiotis LS. Updating models and their uncertainties. I: Bayesian statistical framework. *Journal of Engineering Mechanics ASCE*. 1998;124(4):455-461.
12. Mariani S, Ghisi A. Unscented Kalman filtering for nonlinear structural dynamics. *Nonlinear Dynamics*. 2007;49:131-150.
13. Hasançebi O, Dumlupınar T. Linear and nonlinear model updating of reinforced concrete T-beam bridges using artificial neural networks. *Comput Struct*. 2013;119:1-11.
14. Pordes R et al. The Open Science grid. *Journal of Physics*. 2007;78:012-057.
15. Callaghan S et al. Metrics for heterogeneous scientific workflows: a case study of an earthquake science application. *Int J of High Perform Comput Appl*. 2011;25:274-285.
16. Mazzoni, S., McKenna, F., and Fenves, G.L., 2005. OpenSees command language manual. *http://opensees.berkeley.edu/*. Pacific earthquake engineering research.
17. Boroschek R, Moroni M, Sarrazin M. Dynamic characteristics of a long span seismic isolated bridge. *Eng Struct*. 2003;25:1479-1490.
18. Astroza M, Ruiz S, Astroza R. Damage assessment and seismic intensity analysis of the 2010 (Mw 8.8) Maule earthquake. *Earthq Spectra*. 2012;28(S1):S145-S164.
19. Li, Y., Astroza, R., Conte, J.P., and Soto, P., 2016. Model parameter estimation of a seismic isolated bridge using isolator component test data and bridge response recorded during the 2010 Maule, Chile earthquake. *Report No. SSRP-16/14*, Department of Structural Engineering, University of California, San Diego.
20. Sfiligoi, I., Bradley, D., Burt, H., Parag, M. Sanjay, P., and Frank W., 2009. The pilot way to grid resources using GlideinWMS. *WRI World Congress on Computer Science and Information Engineering*, Los Angeles, CA, 428–432.
21. Gu Q, Barbato M, Conte JP, Gill P, McKenna F. OpenSees-SNOPT framework for finite-element-based optimization of structural and geotechnical systems. *Journal of Structural Engineering ASCE*. 2012;138(6):822-834.
22. Miettinen K. Nonlinear multiobjective optimization. *International Series in Operations Research & Management Science*, vol. 12. New York: Springer; 1998.

How to cite this article: Li Y, Astroza R, Conte JP, Soto P. Nonlinear FE model updating and reconstruction of the response of an instrumented seismic isolated bridge to the 2010 Maule Chile earthquake. *Earthquake Engng Struct Dyn*. 2017;46:2699–2716. https://doi.org/10.1002/eqe.2925